ACS APPLIED ELECTRONIC MATERIALS

pubs.acs.org/acsaelm Article

All-Printed MXene–Graphene Nanosheet-Based Bimodal Sensors for Simultaneous Strain and Temperature Sensing

Mortaza Saeidi-Javash, Yipu Du, Minxiang Zeng, Brian C. Wyatt, Bowen Zhang, Nicholas Kempf, Babak Anasori,* and Yanliang Zhang*

Cite This: https://doi.org/10.1021/acsaelm.1c00218 Read Online

ACCESS | Metrics & More | Article Recommendations | Supporting Information

ABSTRACT: Multifunctional sensors with integrated multiple sensing capabilities have enormous potential for in situ sensing, structural health monitoring, and wearable applications. However, the fabrication of multimodal sensors typically involves complex processing steps, which limit the choices of materials and device form factors. Here, an aerosol jet printed flexible bimodal sensor is demonstrated by using graphene and $Ti_3C_2T_x$ MXene nanoinks. The sensor can detect strain by measuring a change in the AC resistive voltage while simultaneously monitoring temperature by detecting the DC Seebeck voltage across the same printed device pattern. The printed bimodal sensor not only expands the sensing capability beyond conventional single-modality sensors but also provides improved spatial resolution utilizing the microscale printed patterns. The printed temperature sensor shows a competitive thermopower output of 53.6 μV/°C with ultrahigh accuracy and stability during both steady-state and transient thermal cycling tests. The printed sensor also demonstrates excellent flexibility with negligible degradations after 1000 bending cycles. The aerosol jet printing and integration of nanomaterials open many opportunities to design and manufacture multifunctional devices for a broad range of applications.

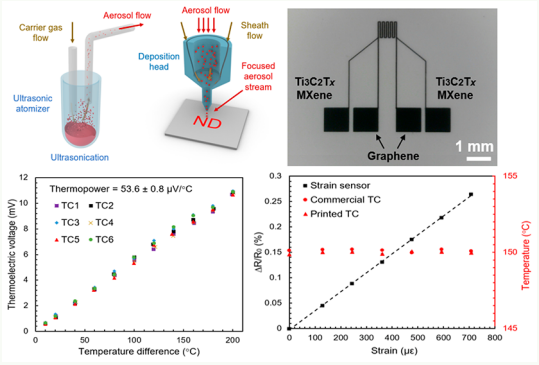

KEYWORDS: *bimodal sensors, aerosol jet printing, multifunctional, graphene, MXene*

1. INTRODUCTION

Printing high-performance flexible strain and temperature sensors has received a significant surge of interest with diverse applications from epidermal sensors to structural health monitoring systems.[1,2] Direct printing techniques such as screen printing, inkjet printing, and aerosol jet printing have attracted tremendous attention due to their abilities to directly convert nanoscale materials into functional devices. Simultaneous sensing of multiple physical quantities is of high value, which allows fabrication of smart human–machine interfaces, soft robotics, and real-time state monitoring of materials degradation and operation conditions in numerous applications.[1,3−7] Significant progresses on printed sensors with a single sensing modality such as strain,[2,8−15] temperature,[16−21] and pressure[22−27] have been made, while sensors with dual or multisensing capabilities remain a challenge due to the complexity of both fabrication processes and decoupling of multiple interfered signals.[28−35] Multimodal sensors require harmonious integration of multiple sensing materials and intimate coupling with the system or physical environment in which the sensor is operating, highlighting the need of implementing novel materials and versatile manufacturing methods for producing multimodal sensors.

Graphene and MXene are two important 2D materials with unique and superior properties for various sensing applications. Since the discovery of graphene in 2004,[36] graphene has been used for a variety of sensing applications such as strain, pressure, and gas sensing.[37,38] MXenes are a large class of transition metal carbides, nitrides, and carbonitrides with a general formula of $M_{n+1}X_nT_x$, where M is an early transition metal (such as Ti, V, Nb, and Mo), X is C and/or N, and T_x represents surface terminations (O, OH, and F).[39,40] Among all the different compositions of MXene, $Ti_3C_2T_x$ has been the most extensively explored MXene for a variety of sensing applications, including strain sensing,[41−44] piezoresistive tactile sensing,[45,46] gas sensing,[47,48] and biosensing.[49−53] Despite the merits of MXenes and graphene individually, the combination of these two materials into one printable multimodal sensing system remains an unexplored avenue. While both MXene and graphene have been demonstrated for strain sensing utilizing

Received: March 7, 2021
Accepted: April 28, 2021

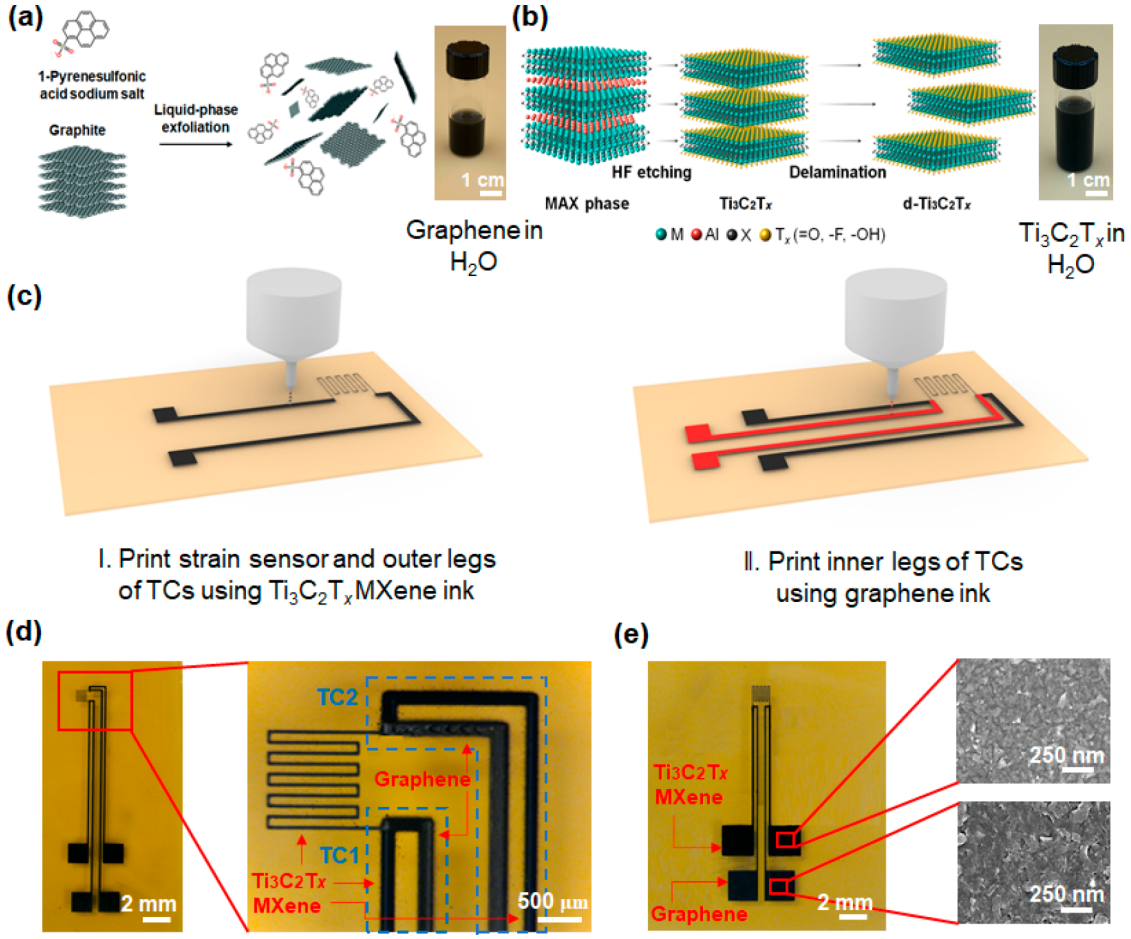

Figure 1. Aerosol jet printing process of bimodal sensors. Schematic illustrations of (a) liquid-phase exfoliation (LPE) of graphite into graphene and (b) selective etching of Ti_3AlC_2 for the preparation of $Ti_3C_2T_x$ MXene. (c) Schematic illustration of the bimodal sensor fabrication process flow including (I) printing the strain sensor and outer legs of the temperature sensors using $Ti_3C_2T_x$ MXene ink and (II) printing the inner legs of temperature sensors using graphene ink. (d) Printed bimodal sensor with horizontal strain sensors. (e) Printed bimodal sensor with vertical strain sensors and top view of SEM images of printed graphene and $Ti_3C_2T_x$ MXene films after annealing.

their conductive nature, their combination provides a new modality for temperature sensing thanks to the differences in their Seebeck coefficients.[54,55] In addition, numerous studies on biocompatibility of these two materials pave the way for potential wearable/implantable applications of the printed bimodal sensors.[51,56−60]

Here, we demonstrate an aerosol jet printed flexible bimodal sensor to simultaneously measure strain from the resistance change of the printed MXene patterns and temperature from the Seebeck voltage at the junction of printed graphene and MXene. The aerosol jet printing (AJP) method was employed to fabricate devices as it can readily process a large variety of nanomaterial-based inks with a relatively wide range of viscosity.[16,61−65] The bimodal sensor shows an improved gauge factor for strain sensing, which is 85% higher than commercial metal strain gauges (e.g., copper−nickel alloy).[11,13] The bimodal sensor demonstrates a competitive thermopower output of 53.6 μV/°C for temperature sensing, while maintaining excellent flexibility and reliability after 1000 bending cycles.

2. RESULTS AND DISCUSSION

Printable graphene inks were synthesized by liquid-phase exfoliation (LPE) of graphite powder in water using pyrene derivatives as stabilizers (Figure 1a), following the method developed previously.[66,67] The lateral sizes of the graphene and MXene flakes are shown in the scanning electron microscopy (SEM) images (Figure S1). The average flake size is 0.67 ± 0.19 and 0.56 ± 0.14 μm, respectively. As shown in Figure 1b, $Ti_3C_2T_x$ MXene nanosheets were prepared by selective etching of Al layers from Ti_3AlC_2 MAX powder with HF/HCl acidic combination (see details in the Experimental Section). The water-based graphene and MXene inks contain their aqueous solutions of 2.9 and 4.8 mg/mL, respectively.

To confirm the intrinsic quality of the 2D flakes before printing, X-ray diffraction (XRD) and Raman spectroscopy were performed on the vacuum-filtered MXene and graphene films. Figure S2 illustrates the XRD spectra of the as-filtered and dried MXene films. XRD data confirm complete selective etching of Ti_3AlC_2 and formation of $Ti_3C_2T_x$.[68] The (002) peaks for these MXene films are around 6.5° and 8.1° for as-filtered and dry $Ti_3C_2T_x$ films (Figure S2), corresponding to an interflake distancing of 13.6 and 11 Å, respectively. The change in the interflake distance of MXene after drying is due to the removal of water molecules from the gallery of MXene flakes. The ratio of D band to G band (I_D/I_G) in Raman spectra (Figure S3) of the annealed graphene films is 31%, confirming the presence of few-layer graphene flakes.[63]

Figure 1c shows the schematic of the aerosol jet printing process of the bimodal sensors on a polyimide (Kapton)

https://doi.org/10.1021/acsaelm.1c00218
ACS Appl. Electron. Mater. XXXX, XXX, XXX−XXX

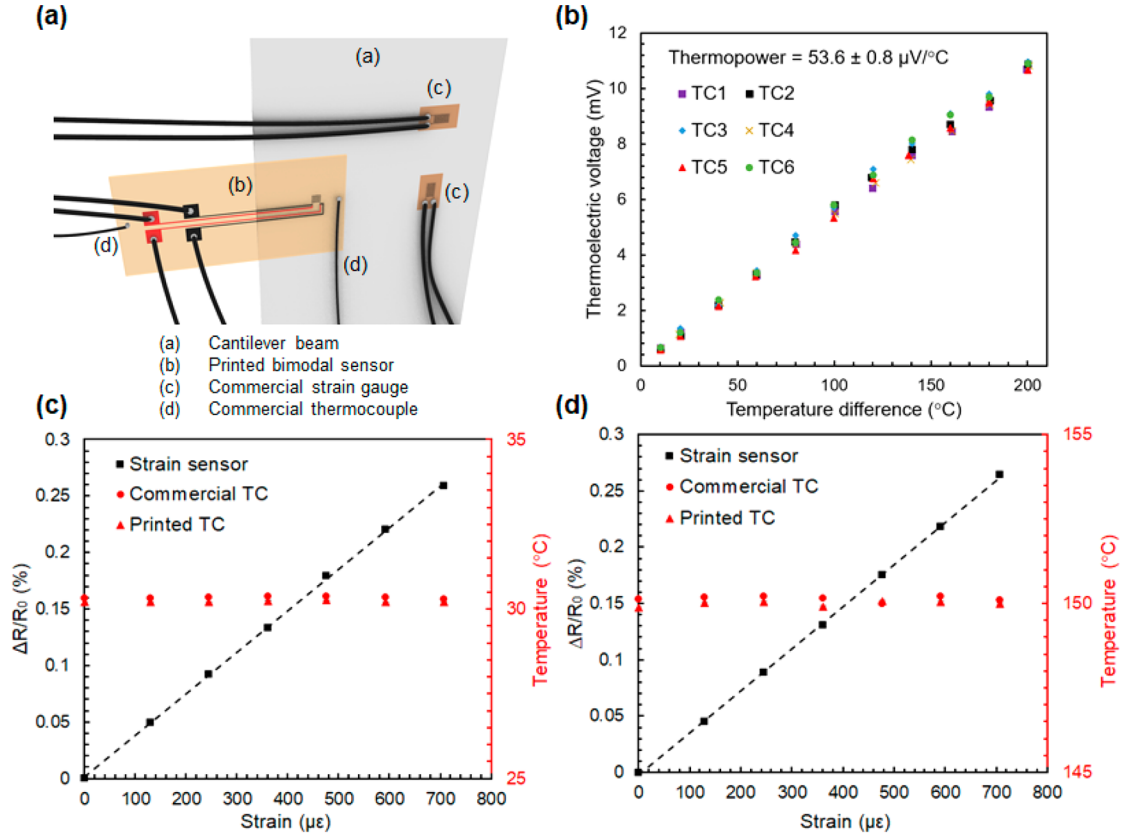

Figure 2. (a) Schematic illustration of the experimental setup showing the cantilever beam, attached bimodal sensor, commercial strain gauges, and commercial K-type thermocouples. (b) Thermoelectric voltage output of the printed bimodal sensor as a function of temperature differences between hot and cold junctions. (c, d) Simultaneous measurement of the strain and temperature at 30.2 and 150 °C, respectively.

substrate. In brief, the cleaned substrate was loaded onto the printer platen, and the strain sensor and the outer legs of thermocouples were printed by using the MXene ink. Then, the inner legs of thermocouples were printed by using the graphene ink. Schematic diagram illustrating the working mechanism of an aerosol jet printer and associated ultrasonic atomizing process is shown in Figure S4, with a detailed description in the Experimental Section. To achieve a printed pattern with the desired line width with minimal overspraying and coffee ring effect, several printing parameters need to be optimized, including the flow rate of the carrier gas that transports the aerosol mist to the substrate, the flow rate of the sheath gas that collimates the aerosol flow into a narrow beam, the nozzle size, the platen temperature, and the printing speed. For example, Figure S5 shows the overspray prior to optimizing the printing parameters. The optimized printing parameters are given in the Supporting Information (Table S1). After printing, the sensors were annealed at 200 °C for 2 h under an inert gas atmosphere (ultrahigh-purity N_2). SEM images of aerosol jet printed graphene and $Ti_3C_2T_x$ films are shown in Figure 1e. Both materials were printed with a single pass, which resulted in film thicknesses of ~0.6 and ~1.35 μm for graphene and $Ti_3C_2T_x$, respectively (Figure S6).

Figure 1d,e shows the images of the printed bimodal sensors with vertical and horizontal strain sensors on polyimide substrates. The bimodal sensor consists of printed MXene with 1 mm^2 active grid area for strain sensing and printed graphene/MXene thermocouple junction (TC1 and TC2) for concurrent temperature sensing. The schematic of the printed bimodal sensors is shown in Figure S7. The printed MXene for strain sensing has a mean width of 40.4 μm with a variation <2% (±0.8 μm) measured at 10 locations (every 100 μm) by an optical microscope and a mean thickness of 0.61 ± 0.01 μm measured by a profilometer (Figure S8). Similarly, the line widths for MXene and graphene thermocouple legs are 122 ± 2 and 122.7 ± 1.6 μm, and their thicknesses are 1.35 ± 0.02 and 0.58 ± 0.03 μm, respectively, which is due to the lower concentration of graphene ink compared to $Ti_3C_2T_x$ MXene (Figure S9). Moreover, 3D confocal microscope images, shown in Figure S10, reveal uniform widths of 128.8 ± 2.5 and 116 ± 2 μm for the printed MXene and graphene legs, respectively. The width variation measured by the confocal microscope agrees within 5% of the measured values by the 2D profilometer.

The concurrent temperature and strain sensing measurements were conducted in air by using an experimental setup shown in Figure 2a. The thermoelectric voltages generated by graphene and $Ti_3C_2T_x$ thermocouple junction were measured under various temperature gradients. The thermoelectric voltage is proportional to the applied temperature gradient and can be written as $V = \int_{T_c}^{T_H} S_G(T) - S_M(T)\, dT$, where S_G and S_M are the temperature-dependent Seebeck coefficients of graphene and MXene legs, respectively, and T_H and T_c are the temperatures of the thermocouple junction and the ambient. As shown in Figure 2b, the thermoelectric voltages of six printed thermocouples (TC1−TC6) increases linearly as a function of the temperature difference between the hot and cold junctions measured by commercial K-type thermocouples (Omega, 36 AWG Wires). The printed thermocouple generates a maximum output voltage of 11 mV under ΔT of

https://doi.org/10.1021/acsaelm.1c00218
ACS Appl. Electron. Mater. XXXX, XXX, XXX−XXX

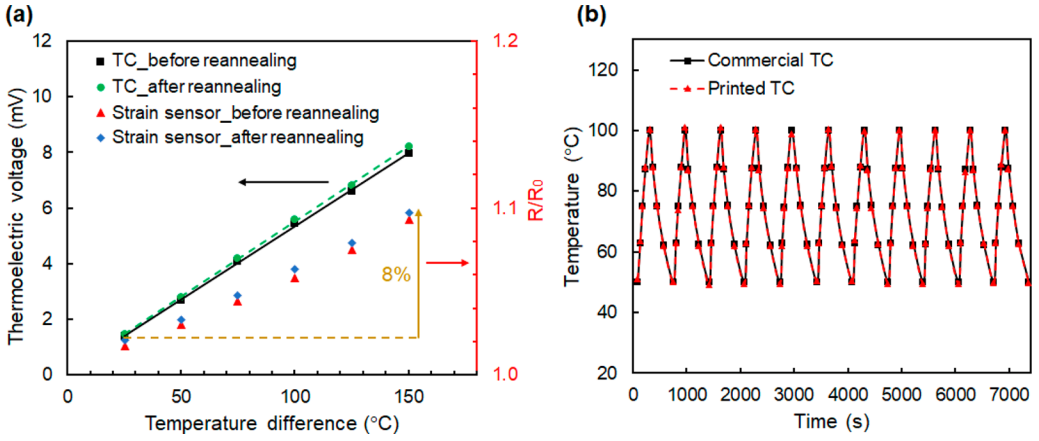

Figure 3. (a) Thermoelectric voltage of the printed thermocouple and relative resistance change of the strain sensor before and after reannealing at 150 °C for 24 h. (b) Repeated cycle test of temperature between 50 and 100 °C.

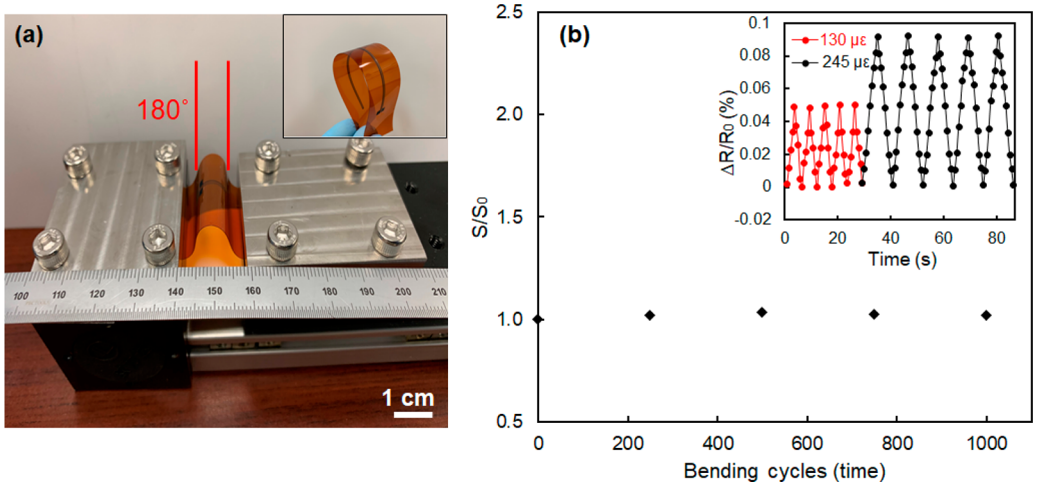

Figure 4. Flexibility test of the printed bimodal sensor. (a) Bending test of the temperature sensor with a bending radius of 5 mm. The inset shows a 10 cm long temperature sensor printed on polyimide. (b) Relative thermopower output change of the temperature sensor at different bending cycles. The inset is a relative resistance change of the strain sensor at room temperature.

200 °C, with a thermopower (i.e., sensitivity) of 53.6 μV/°C across the MXene and graphene junction, which demonstrates a higher sensitivity compared to other film-based thermocouples reported in the literature.[16,35,69−71] Table S2 summarizes the comparison of the thermopower of several nanoparticle-based thermocouples with various methods. Moreover, it is observed that printed thermocouples are very stable in air and retain the same sensitivity and measurement resolution (~0.1 °C) even after 8 months.

To measure the sensor resistance vs strain, the bimodal sensor was attached to a cantilever beam with a standard commercial strain gauge (HBM, LY series) (see details in the Experimental Section). The temperature of the cantilever beam was controlled by using a film heater while the strain was varied by using a motorized linear motion.

A high-frequency (5000 Hz) alternative current (AC) is passed through the printed MXene legs of the thermocouples into the MXene strain sensor, and the strain is detected by measuring the changes of AC resistive voltages between the two printed graphene legs due to the changes of the sensor resistances. The same graphene and MXene legs can be used to simultaneously measure the direct current (DC) Seebeck voltage to obtain temperature. The integrated temperature sensing greatly improves the strain measurement accuracy by decoupling the strain-induced resistance change and the temperature-induced resistance change. The resistance of the strain sensor increases by 8% when the temperature rise reaches 150 °C due to metallic nature of $Ti_3C_2T_x$ MXene, indicating the importance of in situ temperature sensing when using these resistive-based strain sensors (Figure 3a). Figures 2c,d show the concurrent measurements of strain and temperature by the printed bimodal sensor at ~30 and 150 °C. The temperatures measured by the printed thermocouples and the commercial thermocouples agree within 0.5% and 0.1% at ~30 and 150 °C, respectively. Additionally, the gauge factor of the printed strain sensor at both temperatures is 3.7, which is 85% higher than most of the commercial metal strain gauges which typically have a gauge factor around 2.[11,13]

To evaluate the stability of the printed sensors, we performed experiments with regard to their thermal stability and mechanical robustness. For thermal stability, the sensors were reannealed at 150 °C for 24 h under N_2. The thermoelectric voltage generated by the thermocouple and the relative resistance change of the strain sensor were measured before and after reannealing. As shown in Figure 3a, the thermoelectric voltage of the printed thermocouples reveals excellent stability with a slight increase of ~3% at ΔT of 150 °C after reannealing. The resistance of the strain sensor

https://doi.org/10.1021/acsaelm.1c00218
ACS Appl. Electron. Mater. XXXX, XXX, XXX−XXX

increases by <1% at room temperature after reannealing. The performances of the printed bimodal sensor were further evaluated during thermal cycling tests. As shown in Figure 3b, transient temperature measurement of the printed thermocouple during thermal cycling between 50 and 100 °C shows an excellent agreement within 0.7% and 0.1% at 50 and 100 °C with the temperature measured by a commercial K-type thermocouple during 11 thermal cycles (~2 h). It is worth noting that despite the testing in air, both graphene and $Ti_3C_2T_x$ MXene were stable even at ΔT of 200 °C between hot and cold junctions. However, we did not test the sensors above 200 °C because of possible oxidation of $Ti_3C_2T_x$ films at higher temperatures in air,[72] unlike MXene stability under an inert atmosphere.[73]

To assess the mechanical stability and flexibility of the printed bimodal sensor, a bending test was performed by using a motorized linear motion. The printed thermocouple was bent for 1000 cycles with a bending radius of 5 mm, and the sensor performance (thermopower (S), as a function of temperature up to 150 °C) was measured initially and every 250 cycles. As shown in Figure 4, the thermopower change is almost negligible, suggesting that printed thermocouples are mechanically flexible and stable. For the strain sensor, the cantilever beam is periodically deflected (similar to strain measurement in Figures 2c,d) with the strains of 130$\mu\varepsilon$ and 245$\mu\varepsilon$, demonstrating excellent stability with no degradations under repeated loads (Figure 4b, inset). As shown in Figure S11, the strain sensor produces consistent relative resistance change of 0.263 ± 0.001% under a maximum strain of 708$\mu\varepsilon$ over 1000 deflection cycles, which demonstrates good durability of the printed strain sensor.

3. CONCLUSION

In summary, an all-printed thin-film bimodal sensor was fabricated by using graphene and $Ti_3C_2T_x$ nanoinks. The versatile aerosol jet printing method enables the integration of multiple 2D materials into a unique sensor architecture for simultaneous measurement of strain and temperature with superior sensitivity. The integrated temperature sensing with strain sensors facilitates accurate strain measurement without the need for a sophisticated temperature compensation mechanism. In our tested experimental conditions (temperature between 50 and 100 °C and a bending radius of 5 mm), the printed bimodal sensor demonstrates excellent stability and flexibility during thermal cycling and bending cycles. The 3D conformal aerosol jet printing opens the possibility to directly print a microscale sensor network onto 3D curved components for real-time temperature and strain monitoring. This work paves the way for fully printed multifunctional sensors for a broad range of industrial and personalized applications.

4. EXPERIMENTAL SECTION

4.1. Synthesis of Graphene Ink. 1-Pyrenesulfonic acid sodium salt ($C_{16}H_9NaO_3S$, Sigma-Aldrich) was first dissolved in 100 mL of water with a concentration of 0.5 mg/mL, followed by the addition of 300 mg of graphite. The above mixture was then sonicated (Qsonica Q500 sonicator, connected to a chiller, ThermoTeK T257P, to keep the water temperature around 20 °C) for 3 days. After sonication-assisted exfoliation, centrifugation (Thermo Scientific ST8 benchtop centrifuge) was used to remove large and unexfoliated graphite particles. A two-step liquid cascade centrifugation process was used: centrifugation at 2000 RCF for 35 min, collection of supernatants followed by centrifugation at 10000 RCF for 60 min, and redispersion of the sediment (three times).

4.2. Synthesis of $Ti_3C_2T_x$ MXene Ink. The $Ti_3C_2T_x$ MXene ink used in this paper is synthesized from 1 g of its precursor MAX phase Ti_3AlC_2 (Carbon-Ukraine) through selective etching of Al by an acidic mixture composed of 9 mL de-ionized water, 3 mL HF (48% HF Stock, MilliporeSigma), and 18 mL HCl (37% HCl Stock, MilliporeSigma) to comprise a total 30 mL acidic solution. The acidic mixture was placed into a high-density polyethylene (HDPE) container with a magnetic stir bar placed in an oil bath on a Corning 6795-620D digital stirring hot plate. The Ti_3AlC_2 is slowly added (3 min period) and then stirred at 350 rpm at 35 °C for 24 h. After this period, the $Ti_3C_2T_x$ solution is repeatedly washed until the supernatant reaches a pH of 6, via centrifugation with deionized water using an Eppendorf 5804R centrifuge at 3000 RCF for 3 min. After a pH of 6 was achieved, the $Ti_3C_2T_x$ was delaminated by using 1 g of anhydrous LiCl (MilliporeSigma) in 50 mL of deionized water in an HDPE container with a magnetic stir bar in an oil bath for 1 h at 1000 rpm at a temperature of 60 °C. After delamination, the solution is washed of any remaining LiCl similar to the previously defined acid washing steps. Afterword, the delaminated $Ti_3C_2T_x$ solution is centrifuged at 2380 RCF for 1 h, and the supernatant of this cycle is used as the large-flake $Ti_3C_2T_x$ solution. This $Ti_3C_2T_x$ was further concentrated into ink form through centrifugation at 4000 RCF for 30 min. The concentration of the supernatant is determined by vacuum-assisted filtration of 10 mL of solution, overnight drying in a vacuum oven at 100 °C, and then weighing of the final free-standing $Ti_3C_2T_x$ film. For shipping, the $Ti_3C_2T_x$ ink was argon bubbled for 15 min and sealed in aluminum foil and shipped overnight.

4.3. Bimodal Sensor Printing. An aerosol jet printer (AJ 300 system, Optomec, Inc., Albuquerque, NM) was used to print $Ti_3C_2T_x$ MXene and graphene nanoparticle inks. Prior to printing, an AutoCAD schematic design of the bimodal sensor is loaded to the 3D printer to generate a toolpath for printing. The aerosol jet printer includes two atomizers (ultrasonic and pneumatic) which, depending on nanoink viscosity and nanoparticle size, create a mist of droplets with sizes of 1−5 μm. Then the droplets are picked by a carrier gas (N_2) and deposited onto the substrate through the nozzle. A schematic diagram illustrating the working mechanism of an aerosol jet printer and associated ultrasonic atomizing process is shown in Figure S4. We used a polyimide substrate (DuPont Kapton HN, Circleville, OH) with a thickness of 25 μm. Before printing, the polyimide substrate was first washed with deionized water and isopropyl alcohol followed by O_2 plasma treatment for 7 min (Harrick Plasma, PDC-001-HP (115 V), Ithaca, NY). After printing, the bimodal sensors were thermally annealed at 200 °C for 2 h under an inert gas (N_2).

4.4. Calibration of a Cantilever Beam, Strain, and Thermoelectric Voltage Measurement. The cantilever beam is made of aluminum and has dimensions of 300 × 40 × 2.5 mm^3 ($L \times W \times H$). To attach the printed bimodal sensor and commercial strain gauges to the cantilever beam, first, the cantilever beam surface is cleaned by using very fine sandpaper (3M, 400 Grit-X) followed by cleaning using acetone, isopropyl alcohol, and deionized water. After the drying of the beam surface, adhesive (HBM, 250) is applied to the installation spot on the beam and backside of the sensors. Then the adhesive is dried at 160 °C for almost 5 h. For calibrating the cantilever beam, the commercial strain gauge is connected to the Wheatstone bridge, and the output voltage is acquired by using the DAQ system. At a free-standing state, the output voltage generated by the commercial strain gauge is set to zero. Then the cantilever beam is deflected by using a motorized linear motion every 4 mm. The experimental setup is shown in Figure S12. The output voltage is measured at every deflection, and by using the relationship between the output voltage of the Wheatstone bridge and the resistance change of the strain gauge, we calculated the experienced strain by the cantilever beam using the beam theory. The gauge factor of the printed strain sensor is calculated via the following equation:

$$\varepsilon = \frac{\Delta R/R_0}{\mathrm{GF}}$$

https://doi.org/10.1021/acsaelm.1c00218
ACS Appl. Electron. Mater. XXXX, XXX, XXX−XXX

where ε is the strain, $\Delta R/R_0$ is the relative resistance change with respect to the initial reference resistance R_0, and GF is the gauge factor of the sensor provided by the supplier. After calibrating the beam, we used ε to calibrate the printed strain sensor.

The reported thermopower of 53.6 μV/°C in Figure 2b is the average thermopower of six printed thermocouples (TCs) that is calculated by using the student's t distribution at 95% confidence with 1.5% (±0.8 μV/°K) uncertainty, and each TC is measured three times with a standard deviation <5%. The reported resistance change versus strain values in Figures 2c,d are the average of three measurements using a printed strain sensor with a corresponding uncertainty of 8% that is calculated by using the student's t distribution at 95% confidence. Temperature values (both 30.2 and 150 °C) are the average of two TCs, and for each TC the thermoelectric voltage is measured three times with a standard deviation of 4.6%. Similarly, in Figure 3a the average thermoelectric voltage of two printed TCs before and after annealing at 150 °C is reported. For each TC, the thermoelectric voltage is measured three times with a standard deviation of 5%. In Figure 3b, the average transient temperature of two printed thermocouples is compared with a commercial K-type thermocouple during thermal cycling between 50 and 100 °C. In Figure 4, the thermopower of a printed thermocouple is measured over 1000 bending cycles, and the reported thermopower is the average value of three measurements with a standard deviation of 5%.

4.5. Characterizations. Graphene film is characterized by using a micro-Raman microscope (NRS-5100, Jasco) with 532 and 785 nm excitation laser and range 50−8000 cm^{-1}. A scanning electron microscope (Magelllan 400, FEI Company), with working voltage 15 kV and working distance 4.5 mm, is used for cross-section and top-view imaging of the printed graphene and $Ti_3C_2T_x$ MXene films. XRD patterns of wet and dry $Ti_3C_2T_x$ MXene are analyzed by using a Bruker D8 Discover. The width and height variation of printed $Ti_3C_2T_x$ MXene and graphene films are measured by using an Olympus LEXT OLS4100 confocal microscope at the Notre Dame Nanofabrication Facility and DektakXT styles profilometer (Bruker, US).

4.6. $Ti_3C_2T_x$ MXene and Graphene Nanosheets Size Distribution. $Ti_3C_2T_x$ MXene and graphene nanosheets size distribution diagrams are analyzed by using ImageJ software (W.S. Rasband, U.S. National Institutes of Health, Bethesda, MD) based on top-view SEM images. The size distribution for both materials is achieved by measuring the lateral size of 100 individual nanosheets.

■ ASSOCIATED CONTENT

Supporting Information

The Supporting Information is available free of charge at https://pubs.acs.org/doi/10.1021/acsaelm.1c00218.

Nanoparticle size characterization of graphene and $Ti_3C_2T_x$ MXene nanoflakes (Figure S1), XRD patterns of wet and dry $Ti_3C_2T_x$ MXene films (Figure S2), Raman spectra of graphene after annealing at 200 °C for 2 h (Figure S3), schematic diagram illustrating the mechanism of an ultrasonic atomizer and aerosol jet printer deposition head (Figure S4), scanning electron microscopy images of aerosol jet printed films (Figure S6), width and thickness variation of the printed $Ti_3C_2T_x$ MXene strain sensor (Figure S8), width and thickness variation of the printed $Ti_3C_2T_x$ MXene and graphene legs of the TC (Figures S9 and S10), durability test of the printed strain sensor under cyclic deflection (Figure S11), experimental setup (Figure S12), printing parameters (Table S1), and comparison of thermopower of thermocouples fabricated by different techniques (Table S2) (PDF)

■ AUTHOR INFORMATION

Corresponding Authors

Yanliang Zhang − *Department of Aerospace and Mechanical Engineering, University of Notre Dame, Notre Dame, Indiana 46556, United States;* orcid.org/0000-0001-7423-8001; Email: yzhang45@nd.edu

Babak Anasori − *Integrated Nanosystems Development Institute and Department of Mechanical and Energy Engineering, Purdue School of Engineering and Technology, Indiana University−Purdue University Indianapolis, Indianapolis, Indiana 46202, United States;* orcid.org/0000-0002-1955-253X; Email: banasori@iupui.edu

Authors

Mortaza Saeidi-Javash − *Department of Aerospace and Mechanical Engineering, University of Notre Dame, Notre Dame, Indiana 46556, United States*

Yipu Du − *Department of Aerospace and Mechanical Engineering, University of Notre Dame, Notre Dame, Indiana 46556, United States*

Minxiang Zeng − *Department of Aerospace and Mechanical Engineering, University of Notre Dame, Notre Dame, Indiana 46556, United States;* orcid.org/0000-0002-3513-9200

Brian C. Wyatt − *Integrated Nanosystems Development Institute and Department of Mechanical and Energy Engineering, Purdue School of Engineering and Technology, Indiana University−Purdue University Indianapolis, Indianapolis, Indiana 46202, United States*

Bowen Zhang − *Integrated Nanosystems Development Institute and Department of Mechanical and Energy Engineering, Purdue School of Engineering and Technology, Indiana University−Purdue University Indianapolis, Indianapolis, Indiana 46202, United States*

Nicholas Kempf − *Department of Aerospace and Mechanical Engineering, University of Notre Dame, Notre Dame, Indiana 46556, United States*

Complete contact information is available at: https://pubs.acs.org/10.1021/acsaelm.1c00218

Notes

The authors declare no competing financial interest.

■ ACKNOWLEDGMENTS

Y.Z. acknowledges funding support from the National Science Foundation under Award CMMI-1747685 and the U.S. Department of Energy under Awards DE-NE0008712 and DE-NE0008701. We are grateful to Prof. Yury Gogotsi of Drexel University in obtaining the MAX powder and his constructive comments at the start of this project.

■ REFERENCES

(1) Xu, K.; Lu, Y.; Takei, K. Multifunctional Skin-Inspired Flexible Sensor Systems for Wearable Electronics. *Adv. Mater. Technol.* **2019**, *4* (3), 1−25.

(2) Amjadi, M.; Kyung, K. U.; Park, I.; Sitti, M. Stretchable, Skin-Mountable, and Wearable Strain Sensors and Their Potential Applications: A Review. *Adv. Funct. Mater.* **2016**, *26* (11), 1678−1698.

(3) Hou, C.; Wang, H.; Zhang, Q.; Li, Y.; Zhu, M. Highly Conductive, Flexible, and Compressible All-Graphene Passive Electronic Skin for Sensing Human Touch. *Adv. Mater.* **2014**, *26* (29), 5018−5024.

(4) Liu, H.; Xiang, H.; Wang, Y.; Li, Z.; Qian, L.; Li, P.; Ma, Y.; Zhou, H.; Huang, W. A Flexible Multimodal Sensor That Detects Strain, Humidity, Temperature, and Pressure with Carbon Black and Reduced Graphene Oxide Hierarchical Composite on Paper. *ACS Appl. Mater. Interfaces* **2019**, *11* (43), 40613−40619.
(5) Hua, Q.; Sun, J.; Liu, H.; Bao, R.; Yu, R.; Zhai, J.; Pan, C.; Wang, Z. L. Skin-Inspired Highly Stretchable and Conformable Matrix Networks for Multifunctional Sensing. *Nat. Commun.* **2018**, *9* (1), 1−11.
(6) Kim, J.; Lee, M.; Shim, H. J.; Ghaffari, R.; Cho, H. R.; Son, D.; Jung, Y. H.; Soh, M.; Choi, C.; Jung, S.; Chu, K.; Jeon, D.; Lee, S. T.; Kim, J. H.; Choi, S. H.; Hyeon, T.; Kim, D. H. Stretchable Silicon Nanoribbon Electronics for Skin Prosthesis. *Nat. Commun.* **2014**, *5*, 1−11.
(7) An, B. W.; Heo, S.; Ji, S.; Bien, F.; Park, J. U. Transparent and Flexible Fingerprint Sensor Array with Multiplexed Detection of Tactile Pressure and Skin Temperature. *Nat. Commun.* **2018**, *9* (1), 1−10.
(8) Frutiger, A.; Muth, J. T.; Vogt, D. M.; Mengüç, Y.; Campo, A.; Valentine, A. D.; Walsh, C. J.; Lewis, J. A. Capacitive Soft Strain Sensors via Multicore-Shell Fiber Printing. *Adv. Mater.* **2015**, *27* (15), 2440−2446.
(9) Muth, J. T.; Vogt, D. M.; Truby, R. L.; Mengüç, Y.; Kolesky, D. B.; Wood, R. J.; Lewis, J. A. Embedded 3D Printing of Strain Sensors within Highly Stretchable Elastomers. *Adv. Mater.* **2014**, *26* (36), 6307−6312.
(10) Yamada, T.; Hayamizu, Y.; Yamamoto, Y.; Yomogida, Y.; Izadi-Najafabadi, A.; Futaba, D. N.; Hata, K. A Stretchable Carbon Nanotube Strain Sensor for Human-Motion Detection. *Nat. Nanotechnol.* **2011**, *6* (5), 296−301.
(11) Rahman, M. T.; Moser, R.; Zbib, H. M.; Ramana, C. V.; Panat, R. 3D Printed High Performance Strain Sensors for High Temperature Applications. *J. Appl. Phys.* **2018**, *123*, 024501−11.
(12) Zhao, S.; Li, J.; Cao, D.; Zhang, G.; Li, J.; Li, K.; Yang, Y.; Wang, W.; Jin, Y.; Sun, R.; Wong, C. P. Recent Advancements in Flexible and Stretchable Electrodes for Electromechanical Sensors: Strategies, Materials, and Features. *ACS Appl. Mater. Interfaces* **2017**, *9* (14), 12147−12164.
(13) Zhang, Y.; Anderson, N.; Bland, S.; Nutt, S.; Jursich, G.; Joshi, S. All-Printed Strain Sensors: Building Blocks of the Aircraft Structural Health Monitoring System. *Sens. Actuators, A* **2017**, *253*, 165−172.
(14) Borghetti, M.; Serpelloni, M.; Sardini, E. Printed Strain Gauge on 3D and Low-Melting Point Plastic Surface by Aerosol Jet Printing and Photonic Curing. *Sensors* **2019**, *19* (19), 4220.
(15) Agarwala, S.; Goh, G. L.; Yeong, W. Y. Aerosol Jet Printed Strain Sensor: Simulation Studies Analyzing the Effect of Dimension and Design on Performance (September 2018). *IEEE Access* **2018**, *6*, 63080−63086.
(16) Rahman, M. T.; Cheng, C. Y.; Karagoz, B.; Renn, M.; Schrandt, M.; Gellman, A.; Panat, R. High Performance Flexible Temperature Sensors via Nanoparticle Printing. *ACS Appl. Nano Mater.* **2019**, *2* (5), 3280−3291.
(17) Yokota, T.; Inoue, Y.; Terakawa, Y.; Reeder, J.; Kaltenbrunner, M.; Ware, T.; Yang, K.; Mabuchi, K.; Murakawa, T.; Sekino, M.; Voit, W.; Sekitani, T.; Someya, T. Ultraflexible, Large-Area, Physiological Temperature Sensors for Multipoint Measurements. *Proc. Natl. Acad. Sci. U. S. A.* **2015**, *112* (47), 14533−14538.
(18) Harada, S.; Kanao, K.; Yamamoto, Y.; Arie, T.; Akita, S.; Takei, K. Fully Printed Flexible Fingerprint-like Three-Axis Tactile and Slip Force and Temperature Sensors for Artificial Skin. *ACS Nano* **2014**, *8* (12), 12851−12857.
(19) Aliane, A.; Fischer, V.; Galliari, M.; Tournon, L.; Gwoziecki, R.; Serbutoviez, C.; Chartier, I.; Coppard, R. Enhanced Printed Temperature Sensors on Flexible Substrate. *Microelectron. J.* **2014**, *45* (12), 1621−1626.
(20) Katerinopoulou, D.; Zalar, P.; Sweelssen, J.; Kiriakidis, G.; Rentrop, C.; Groen, P.; Gelinck, G. H.; van den Brand, J.; Smits, E. C. P. Large-Area All-Printed Temperature Sensing Surfaces Using Novel Composite Thermistor Materials. *Adv. Electron. Mater.* **2019**, *5* (2), 1−7.
(21) Dankoco, M. D.; Tesfay, G. Y.; Benevent, E.; Bendahan, M. Temperature Sensor Realized by Inkjet Printing Process on Flexible Substrate. *Mater. Sci. Eng., B* **2016**, *205*, 1−5.
(22) Mannsfeld, S. C. B.; Tee, B. C. K.; Stoltenberg, R. M.; Chen, C. V. H. H.; Barman, S.; Muir, B. V. O.; Sokolov, A. N.; Reese, C.; Bao, Z. Highly Sensitive Flexible Pressure Sensors with Microstructured Rubber Dielectric Layers. *Nat. Mater.* **2010**, *9* (10), 859−864.
(23) Lee, S.; Reuveny, A.; Reeder, J.; Lee, S.; Jin, H.; Liu, Q.; Yokota, T.; Sekitani, T.; Isoyama, T.; Abe, Y.; Suo, Z.; Someya, T. A Transparent Bending-Insensitive Pressure Sensor. *Nat. Nanotechnol.* **2016**, *11* (5), 472−478.
(24) Khan, Y.; Ostfeld, A. E.; Lochner, C. M.; Pierre, A.; Arias, A. C. Monitoring of Vital Signs with Flexible and Wearable Medical Devices. *Adv. Mater.* **2016**, *28* (22), 4373−4395.
(25) Austin, J. H. References and Notes. *Meditating Selflessly* **2019**, 952−958.
(26) Han, S.; Kim, J.; Won, S. M.; Ma, Y.; Kang, D.; Xie, Z.; Lee, K. T.; Chung, H. U.; Banks, A.; Min, S.; Heo, S. Y.; Davies, C. R.; Lee, J. W.; Lee, C. H.; Kim, B. H.; Li, K.; Zhou, Y.; Wei, C.; Feng, X.; Huang, Y.; Rogers, J. A. Battery-Free, Wireless Sensors for Full-Body Pressure and Temperature Mapping. *Sci. Transl. Med.* **2018**, *10* (435), 1−13.
(27) Gong, S.; Schwalb, W.; Wang, Y.; Chen, Y.; Tang, Y.; Si, J.; Shirinzadeh, B.; Cheng, W. A Wearable and Highly Sensitive Pressure Sensor with Ultrathin Gold Nanowires. *Nat. Commun.* **2014**, *5*, 1−8.
(28) Jung, M.; Kim, K.; Kim, B.; Cheong, H.; Shin, K.; Kwon, O. S.; Park, J. J.; Jeon, S. Paper-Based Bimodal Sensor for Electronic Skin Applications. *ACS Appl. Mater. Interfaces* **2017**, *9* (32), 26974−26982.
(29) Liu, Y.; Wang, H.; Zhao, W.; Zhang, M.; Qin, H.; Xie, Y. Flexible, Stretchable Sensors for Wearable Health Monitoring: Sensing Mechanisms, Materials, Fabrication Strategies and Features. *Sensors* **2018**, *18* (2), 1−35.
(30) Boutry, C. M.; Negre, M.; Jorda, M.; Vardoulis, O.; Chortos, A.; Khatib, O.; Bao, Z. A Hierarchically Patterned, Bioinspired e-Skin Able to Detect the Direction of Applied Pressure for Robotics. *Sci. Robot.* **2018**, *3* (24), 1−10.
(31) Choi, D.; Jang, S.; Kim, J. S.; Kim, H. J.; Kim, D. H.; Kwon, J. Y. A Highly Sensitive Tactile Sensor Using a Pyramid-Plug Structure for Detecting Pressure, Shear Force, and Torsion. *Adv. Mater. Technol.* **2019**, *4* (3), 1−10.
(32) Harada, S.; Honda, W.; Arie, T.; Akita, S.; Takei, K. Fully Printed, Highly Sensitive Multifunctional Artificial Electronic Whisker Arrays Integrated with Strain and Temperature Sensors. *ACS Nano* **2014**, *8* (4), 3921−3927.
(33) Fu, S.; Tao, J.; Wu, W.; Sun, J.; Li, F.; Li, J.; Huo, Z.; Xia, Z.; Bao, R.; Pan, C. Fabrication of Large-Area Bimodal Sensors by All-Inkjet-Printing. *Adv. Mater. Technol.* **2019**, *4* (4), 1−9.
(34) Won, S. M.; Wang, H.; Kim, B. H.; Lee, K.; Jang, H.; Kwon, K.; Han, M.; Crawford, K. E.; Li, H.; Lee, Y.; Yuan, X.; Kim, S. B.; Oh, Y. S.; Jang, W. J.; Lee, J. Y.; Han, S.; Kim, J.; Wang, X.; Xie, Z.; Zhang, Y.; Huang, Y.; Rogers, J. A. Multimodal Sensing with a Three-Dimensional Piezoresistive Structure. *ACS Nano* **2019**, *13* (10), 10972−10979.
(35) Knoll, M.; Offenzeller, C.; Mayrhofer, B.; Jakoby, B.; Hilber, W. A Screen Printed Thermocouple-Array on a Flexible Substrate for Condition Monitoring. *Proceedings* **2018**, *2* (13), 803.
(36) Novoselov, K. S.; Geim, A. K.; Morozov, S. V.; Jiang, D.; Zhang, Y.; Dubonos, S. V.; G, I. V.; F, A. A. *Science* **2004**, *306* (5696), 666−669.
(37) Novoselov, K. S.; Fal'Ko, V. I.; Colombo, L.; Gellert, P. R.; Schwab, M. G.; Kim, K. A Roadmap for Graphene. *Nature* **2012**, *490* (7419), 192−200.
(38) Jabari, E.; Ahmed, F.; Liravi, F.; Secor, E. B.; Lin, L.; Toyserkani, E. 2D Printing of Graphene: A Review. *2D Mater.* **2019**, *6* (4), 042004.
(39) Naguib, M.; Kurtoglu, M.; Presser, V.; Lu, J.; Niu, J.; Heon, M.; Hultman, L.; Gogotsi, Y.; Barsoum, M. W. Two-Dimensional

https://doi.org/10.1021/acsaelm.1c00218
ACS Appl. Electron. Mater. XXXX, XXX, XXX−XXX

Nanocrystals Produced by Exfoliation of Ti 3AlC 2. *Adv. Mater.* **2011**, *23* (37), 4248−4253.
(40) Anasori, B.; Lukatskaya, M. R.; Gogotsi, Y. 2D Metal Carbides and Nitrides (MXenes) for Energy Storage. *Nat Rev Mater* **2017**, *2*, 16098.
(41) Hantanasirisakul, K.; Gogotsi, Y. Electronic and Optical Properties of 2D Transition Metal Carbides and Nitrides (MXenes). *Adv. Mater.* **2018**, *30* (52), 1−30.
(42) Cai, Y.; Shen, J.; Ge, G.; Zhang, Y.; Jin, W.; Huang, W.; Shao, J.; Yang, J.; Dong, X. Stretchable Ti3C2Tx MXene/Carbon Nanotube Composite Based Strain Sensor with Ultrahigh Sensitivity and Tunable Sensing Range. *ACS Nano* **2018**, *12* (1), 56−62.
(43) Zhang, Y. Z.; Lee, K. H.; Anjum, D. H.; Sougrat, R.; Jiang, Q.; Kim, H.; Alshareef, H. N. MXenes Stretch Hydrogel Sensor Performance to New Limits. *Sci. Adv.* **2018**, *4* (6), 1−8.
(44) Shi, X.; Wang, H.; Xie, X.; Xue, Q.; Zhang, J.; Kang, S.; Wang, C.; Liang, J.; Chen, Y. Bioinspired Ultrasensitive and Stretchable MXene-Based Strain Sensor via Nacre-Mimetic Microscale "Brick-and-Mortar" Architecture. *ACS Nano* **2019**, *13* (1), 649−659.
(45) Ma, Y.; Liu, N.; Li, L.; Hu, X.; Zou, Z.; Wang, J.; Luo, S.; Gao, Y. A Highly Flexible and Sensitive Piezoresistive Sensor Based on MXene with Greatly Changed Interlayer Distances. *Nat. Commun.* **2017**, *8* (1), 1−7.
(46) Li, X.-P.; Li, Y.; Li, X.; Song, D.; Min, P.; Hu, C.; Zhang, H.-B.; Koratkar, N.; Yu, Z.-Z. Highly Sensitive, Reliable and Flexible Piezoresistive Pressure Sensors Featuring Polyurethane Sponge Coated with MXene Sheets. *J. Colloid Interface Sci.* **2019**, *542*, 54−62.
(47) Ma, Y.; Yue, Y.; Zhang, H.; Cheng, F.; Zhao, W.; Rao, J.; Luo, S.; Wang, J.; Jiang, X.; Liu, Z.; Liu, N.; Gao, Y. 3D Synergistical MXene/Reduced Graphene Oxide Aerogel for a Piezoresistive Sensor. *ACS Nano* **2018**, *12* (4), 3209−3216.
(48) Kim, S. J.; Koh, H. J.; Ren, C. E.; Kwon, O.; Maleski, K.; Cho, S. Y.; Anasori, B.; Kim, C. K.; Choi, Y. K.; Kim, J.; Gogotsi, Y.; Jung, H. T. Metallic Ti3C2Tx MXene Gas Sensors with Ultrahigh Signal-to-Noise Ratio. *ACS Nano* **2018**, *12* (2), 986−993.
(49) Wang, F.; Yang, C. H.; Duan, C. Y.; Xiao, D.; Tang, Y.; Zhu, J. F. An Organ-like Titanium Carbide Material (MXene) with Multilayer Structure Encapsulating Hemoglobin for a Mediator-Free Biosensor. *J. Electrochem. Soc.* **2015**, *162* (1), B16−B21.
(50) Liu, H.; Duan, C.; Yang, C.; Shen, W.; Wang, F.; Zhu, Z. A Novel Nitrite Biosensor Based on the Direct Electrochemistry of Hemoglobin Immobilized on MXene-Ti3C2. *Sens. Actuators, B* **2015**, *218*, 60−66.
(51) Rasool, K.; Helal, M.; Ali, A.; Ren, C. E.; Gogotsi, Y.; Mahmoud, K. A. Antibacterial Activity of Ti3C2Tx MXene. *ACS Nano* **2016**, *10* (3), 3674−3684.
(52) Lee, E.; Vahidmohammadi, A.; Prorok, B. C.; Yoon, Y. S.; Beidaghi, M.; Kim, D. J. Room Temperature Gas Sensing of Two-Dimensional Titanium Carbide (MXene). *ACS Appl. Mater. Interfaces* **2017**, *9* (42), 37184−37190.
(53) Chen, X.; Sun, X.; Xu, W.; Pan, G.; Zhou, D.; Zhu, J.; Wang, H.; Bai, X.; Dong, B.; Song, H. Ratiometric Photoluminescence Sensing Based on Ti3C2MXene Quantum Dots as an Intracellular PH Sensor. *Nanoscale* **2018**, *10* (3), 1111−1118.
(54) Juntunen, T.; Jussila, H.; Ruoho, M.; Liu, S.; Hu, G.; Albrow-Owen, T.; Ng, L. W. T.; Howe, R. C. T.; Hasan, T.; Sun, Z.; Tittonen, I. Inkjet Printed Large-Area Flexible Few-Layer Graphene Thermoelectrics. *Adv. Funct. Mater.* **2018**, *28* (22), 1800480.
(55) Jiang, X.; Kuklin, A. V.; Baev, A.; Ge, Y.; Ågren, H.; Zhang, H.; Prasad, P. N. Two-Dimensional MXenes: From Morphological to Optical, Electric, and Magnetic Properties and Applications. *Phys. Rep.* **2020**, *848*, 1−58.
(56) Basara, G.; Saeidi-Javash, M.; Ren, X.; Bahcecioglu, G.; Wyatt, B. C.; Anasori, B.; Zhang, Y.; Zorlutuna, P. Electrically Conductive 3D Printed Ti3C2Tx MXene-PEG Composite Constructs for Cardiac Tissue Engineering. *Acta Biomater.* **2020**.
(57) Dai, C.; Chen, Y.; Jing, X.; Xiang, L.; Yang, D.; Lin, H.; Liu, Z.; Han, X.; Wu, R. Two-Dimensional Tantalum Carbide (MXenes) Composite Nanosheets for Multiple Imaging-Guided Photothermal Tumor Ablation. *ACS Nano* **2017**, *11* (12), 12696−12712.
(58) Liu, G.; Zou, J.; Tang, Q.; Yang, X.; Zhang, Y.; Zhang, Q.; Huang, W.; Chen, P.; Shao, J.; Dong, X. Surface Modified Ti3C2MXene Nanosheets for Tumor Targeting Photothermal/Photodynamic/Chemo Synergistic Therapy. *ACS Appl. Mater. Interfaces* **2017**, *9* (46), 40077−40086.
(59) Syama, S.; Mohanan, P. V. Safety and Biocompatibility of Graphene: A New Generation Nanomaterial for Biomedical Application. *Int. J. Biol. Macromol.* **2016**, *86*, 546−555.
(60) Wu, X.; Ding, S. J.; Lin, K.; Su, J. A Review on the Biocompatibility and Potential Applications of Graphene in Inducing Cell Differentiation and Tissue Regeneration. *J. Mater. Chem. B* **2017**, *5* (17), 3084−3102.
(61) Hammock, M. L.; Chortos, A.; Tee, B. C. K.; Tok, J. B. H.; Bao, Z. 25th Anniversary Article: The Evolution of Electronic Skin (E-Skin): A Brief History, Design Considerations, and Recent Progress. *Adv. Mater.* **2013**, *25* (42), 5997−6038.
(62) Saeidi-Javash, M.; Kuang, W.; Dun, C.; Zhang, Y. 3D Conformal Printing and Photonic Sintering of High-Performance Flexible Thermoelectric Films Using 2D Nanoplates. *Adv. Funct. Mater.* **2019**, *29* (35), 3−8.
(63) Jabari, E.; Toyserkani, E. Micro-Scale Aerosol-Jet Printing of Graphene Interconnects. *Carbon* **2015**, *91*, 321−329.
(64) Rahman, M. T.; Rahimi, A.; Gupta, S.; Panat, R. Microscale Additive Manufacturing and Modeling of Interdigitated Capacitive Touch Sensors. *Sens. Actuators, A* **2016**, *248*, 94−103.
(65) Saleh, M. S.; Hu, C.; Panat, R. Three-Dimensional Micro-architected Materials and Devices Using Nanoparticle Assembly by Pointwise Spatial Printing. *Sci. Adv.* **2017**, *3* (3), e1601986.
(66) Hernandez, Y.; Nicolosi, V.; Lotya, M.; Blighe, F. M.; Sun, Z.; De, S.; McGovern, I. T.; Holland, B.; Byrne, M.; Gun'Ko, Y. K.; Boland, J. J.; Niraj, P.; Duesberg, G.; Krishnamurthy, S.; Goodhue, R.; Hutchison, J.; Scardaci, V.; Ferrari, A. C.; Coleman, J. N. High-Yield Production of Graphene by Liquid-Phase Exfoliation of Graphite. *Nat. Nanotechnol.* **2008**, *3*, 563.
(67) Nicolosi, V.; Chhowalla, M.; Kanatzidis, M. G.; Strano, M. S.; Coleman, J. N. Liquid Exfoliation of Layered Materials. *Science (Washington, DC, U. S.)* **2013**, *340* (6139), 1226419.
(68) Someya, T.; Sekitani, T.; Iba, S.; Kato, Y.; Kawaguchi, H.; Sakurai, T. A Large-Area, Flexible Pressure Sensor Matrix with Organic Field-Effect Transistors for Artificial Skin Applications. *Proc. Natl. Acad. Sci. U. S. A.* **2004**, *101* (27), 9966−9970.
(69) Yang, F.; Li, G.; Yang, J.; Wang, Z.; Han, D.; Zheng, F.; Xu, S. Measurement of Local Temperature Increments Induced by Cultured HepG2 Cells with Micro-Thermocouples in a Thermally Stabilized System. *Sci. Rep.* **2017**, *7* (1), 1−12.
(70) Murakami, R.; Kamada, K.; Shoji, Y.; Yokota, Y.; Yoshino, M.; Kurosawa, S.; Ohashi, Y.; Yamaji, A.; Yoshikawa, A. Fabrication of Flexible Ir and Ir-Rh Wires and Application for Thermocouple. *J. Cryst. Growth* **2018**, *487*, 72−77.
(71) Li, F.; Liu, Y.; Shi, X.; Li, H.; Wang, C.; Zhang, Q.; Ma, R.; Liang, J. Printable and Stretchable Temperature-Strain Dual-Sensing Nanocomposite with High Sensitivity and Perfect Stimulus Discriminability. *Nano Lett.* **2020**, *20* (8), 6176−6184.
(72) Zhang, C. J.; Pinilla, S.; McEvoy, N.; Cullen, C. P.; Anasori, B.; Long, E.; Park, S. H.; Seral-Ascaso, A.; Shmeliov, A.; Krishnan, D.; Morant, C.; Liu, X.; Duesberg, G. S.; Gogotsi, Y.; Nicolosi, V. Oxidation Stability of Colloidal Two-Dimensional Titanium Carbides (MXenes). *Chem. Mater.* **2017**, *29* (11), 4848−4856.
(73) Seredych, M.; Shuck, C. E.; Pinto, D.; Alhabeb, M.; Precetti, E.; Deysher, G.; Anasori, B.; Kurra, N.; Gogotsi, Y. High-Temperature Behavior and Surface Chemistry of Carbide MXenes Studied by Thermal Analysis. *Chem. Mater.* **2019**, *31* (9), 3324−3332.

https://doi.org/10.1021/acsaelm.1c00218
ACS Appl. Electron. Mater. XXXX, XXX, XXX−XXX